	Effects of Alkyl Side Chain Length on the Structural			
Title	Organization and Proton Conductivity of Sulfonated			
	Polyimide Thin Films			
Author(s)	Honbo, Tetsuya; Ono, Yutaro; Suetsugu, Kota; Hara,			
	Mitsuo; Taborosi, Attila; Aoki, Kentaro; Nagano,			
	Shusaku; Koyama, Michihisa; Nagao, Yuki			
O'' ''	ACS Applied Polymer Materials, 6(21): 13217-			
Citation	13227			
Issue Date	2024-10-21			
issue Date	2024-10-21			
Туре	Journal Article			
Text version	author			
URL	http://hdl.handle.net/10119/20021			
	Tetsuya Honbo, Yutaro Ono, Kota Suetsugu, Mitsuo			
	Hara, Attila Taborosi, Kentaro Aoki, Shusaku			
	Nagano, Michihisa Koyama, and Yuki Nagao, ACS			
	, ,			
	Applied Polymer Materials, 2024, 6, 21, 13217-			
	Applied Polymer Materials, 2024, 6, 21, 13217- 13227. This document is the Accepted Manuscript			
Rights				
Rights	13227. This document is the Accepted Manuscript			
Rights	13227. This document is the Accepted Manuscript version of a Published Work that appeared in final			
Rights	13227. This document is the Accepted Manuscript version of a Published Work that appeared in final form in ACS Applied Polymer Materials, copyright			
Rights	13227. This document is the Accepted Manuscript version of a Published Work that appeared in final form in ACS Applied Polymer Materials, copyright (c) American Chemical Society after peer review			
Rights	13227. This document is the Accepted Manuscript version of a Published Work that appeared in final form in ACS Applied Polymer Materials, copyright (c) American Chemical Society after peer review and technical editing by the publisher. To access			



Effects of Alkyl Side Chain Length on the Structural Organization and Proton Conductivity of Sulfonated Polyimide Thin Films

Tetsuya Honbo,^a Yutaro Ono,^a Kota Suetsugu,^b Mitsuo Hara,^b Attila Taborosi,^c Kentaro Aoki,^a Shusaku Nagano,^d Michihisa Koyama,^c and Yuki Nagao^{a*}

^aSchool of Materials Science, Japan Advanced Institute of Science and Technology, 1-1 Asahidai, Nomi, Ishikawa 923-1292, Japan

^bDepartment of Molecular Design & Engineering, Graduate School of Engineering, Nagoya University, Furo-cho, Chikusa, Nagoya, Aichi 464-8603, Japan

^cResearch Initiative for Supra-Materials, Shinshu University, 4-17-1 Wakasato, Nagano 380-8553, Japan

^dDepartment of Chemistry, College of Science, Rikkyo University, 3-34-1 Nishi-ikebukuro, Toshima, Tokyo 171-8501, Japan

KEYWORDS lyotropic liquid crystalline properties, aligned structure, proton dissociation, universal neural network potential, proton transport mechanisms

Abstract

This study investigates the impact of alkyl side chain length on structural organization and proton conductivity of sulfonated polyimide (SPI) thin films. SPIs with different alkyl sulfonated side chain lengths \mathbf{CX} (\mathbf{X} : number of carbon atoms at the side chain, $\mathbf{X}=0$, 3, 6 and 10) were synthesized and the relationship between molecular architecture and proton transport properties was investigated. In all SPIs, the polymer backbone oriented parallel to the substrate, and the lamellar structures were confirmed, with spacing increasing linearly with side chain length. Water uptake behavior and proton conductivity varied significantly, where $\mathbf{C0}$ thin film exhibited the highest water uptake and proton conductivity at lower humidity. While, $\mathbf{C3}$ thin film achieved higher conductivity under high humidity, reaching 1.8×10^{-1} S cm⁻¹ at 298 K and 95% relative humidity (RH) and the activation energy of 0.18 eV at 90% RH. Conversely, extending the alkyl side chain length led to the insolubility in water in $\mathbf{C10}$. As a result, a proton exchange membrane system with high chemical/water stability and high proton conductivity was constructed. These findings provide critical insights into designing advanced proton-conducting materials, optimizing their performance for fuel cells and other electrochemical devices.

1. Introduction

Proton-conducting polymers are essential materials in various applications due to their ability to efficiently conduct protons.¹ These materials are particularly valuable for energy conversion

technologies, where their unique molecular architecture facilitates ion transport through phase-segregated hydrophilic and hydrophobic domains, coupled with water-absorption capabilities.¹⁻² Many polymers exhibiting proton conductivity have been widely reported and thoroughly investigated. The structure of these polymers relies on phase segregation, which separates hydrophobic and hydrophilic domains, along with the ability to absorb water. Proton transport primarily takes place through the hydrophilic regions of these materials.²⁻¹⁰ Recent advancements in this field have highlighted the significance of structural organization and molecular orientation, which can be influenced by intrinsic molecular interactions and external environmental conditions such as hydrogen bonds, hydrophobic effects, pressure, electric fields, magnetic fields, and photo-irradiation.¹¹⁻¹³

For instance, Ichikawa *et al.* designed gemini-type zwitterionic amphiphiles for creating gyroid nanostructured proton conductive membranes using a liquid crystalline (LC) property and proposed surface proton hopping conduction mechanism.¹⁴⁻¹⁵ Luo *et al.* demonstrated that well-defined lamellar liquid crystals exhibited markedly higher proton conductivity compared to micellar solutions.¹⁶ They used 1-tetradecyl-3-methylimidazolium hydrogen sulfate in aqueous solutions and found that the lamellar lyotropic liquid crystals exhibited a proton conductivity of 0.21 S cm⁻¹ at 25 °C, significantly higher than that of micellar solutions under the same conditions. Similarly, Yao *et al.* synthesized sulfonated semialicyclic oligoimides that formed a loosely packed lamellar structure under humidified conditions, demonstrating remarkable proton conductivity reaching 0.2 S cm⁻¹ at 298 K and 95% relative humidity (RH).¹⁷ This high conductivity was attributed to the organized lamellar structure facilitated by the linear conformation of the backbone. Additionally, Goto *et al.* prepared and structurally characterized shear-aligned films of high proton conductive alkyl-sulfonated polyimides with lyotropic LC

properties. Their study showed that aligning the polymer chains in the in-plane (IP) direction of the film significantly enhanced proton conductivity, achieving up to 10^{-1} S cm⁻¹ at 298 K and 95% RH.¹⁸

One promising approach involves the use of sulfonated polyimides (SPIs), which can form organized lamellar structures upon hydration by lyotropic LC properties. These lamellar structures significantly impact proton transport properties, making them a focal point for optimizing the performance of proton-conducting materials. Incorporating LC properties into polymer design offers a promising avenue for enhancing proton conductivity. Despite their potential, the relationship between the molecular organized structure of SPIs, specifically the length of alkyl side chains, and their proton conductivity remains underexplored. Understanding this relationship is vital for optimizing the design of SPIs for high-performance proton-conducting applications. Previous studies have highlighted that the organizational structure of polymer electrolytes, including the formation of lamellar structures and the alignment of polymer backbones, significantly influences proton transport. The length of alkyl side chains can affect the spacing between lamellar and the overall morphology of the polymer, which in turn impacts the material's proton conductivity.

The objective is to provide insights into how side chain length **X** (**X** = 0, 3, 6, 10) in the polymer **CX** influences the formation of lamellar structures as shown in Figure 1, water uptake, proton dissociation, and proton transport properties using a combination of analytical techniques, including polarized optical microscopy (POM), infrared p-polarized multiple angle incidence resolution spectrometry (pMAIRS),²²⁻²³ in situ quartz crystal microbalance (QCM), in situ grazing-incidence X-ray scattering (GIXRS), and in situ Fourier transform infrared (FTIR) measurements. By manipulating the alkyl side chain length, this study seeks to elucidate the relationship between

molecular organization and proton transport efficiency, guiding the development of advanced materials for various electrochemical applications such as fuel cells, electrolyzers, and sensors. The results from this research will contribute to a deeper understanding of the impact of alkyl side chain length on the structural organization and proton conductivity of SPIs, thereby optimizing their performance in practical applications. These findings will help in designing more efficient and cost-effective proton-conducting materials, addressing some of the limitations of current polymer electrolytes.

Figure 1. Chemical structure of SPIs in this study. NTDA-BDSA (**C0**), NTDA-BSPB (**C3**),²¹ NTDA-BSHB (**C6**), and NTDA-BSDB (**C10**). (NTDA: 1,4,5,8-Naphthalenetetracarboxylic dianhydride, BDSA: 2,2'-benzidinedisulfonic acid, BSPB: 3,3'-bis(sulfopropoxy)benzidine, BSHB: 3,3'-bis(6-sulfohexyloxy)benzidine, BSDB: 3,3'-bis(10-sulfodecyloxy)benzidine)

2. Experimental

2. 1 Materials

1,10-Dibromodecane (95.0%), 1,6-dibromohexane (97.0%), 3,3'-dihydroxybenzidine (99.0%), and 2,2'-benzidinedisulfonic acid (contains 30% water at maximum, 70.0%) were purchased from Tokyo Chemical Industry Co., Ltd. 2-Propanol (99.7%), acetic acid (99.7%), acetic anhydride (97.0%), acetone (99.0%), acetonitrile (99.5%), chloroform (99.0%), ethanol (99.5%), ethyl acetate (99.5%), hexane (96.0%), hydrochloric acid (35.0-37.0%), iron(II) sulfate heptahydrate (99.0%), m-cresol (98.0%), N,N'-dimethylformamide (HPLC grade), potassium carbonate anhydrous (99.0%), and sodium sulfite (97.0%) were purchased from Fujifilm Wako Pure Chemical Corporation. 1,4,5,8-Naphthalenetetracarboxylic dianhydride (NTDA) (\leq 100%) was purchased from Sigma-Aldrich. Triethylamine (99.0%) and sodium nitrate were purchased from Kanto Chemical Co., Inc. Hydrogen peroxide (35%) was purchased from Nacalai Tesque, Inc. All reagents were used without further purification otherwise noted.

2.2. Synthesis of Alkyl-Sulfonated Polyimides with Varying Side Chain Lengths

2.2.1. Synthesis of C0

The synthetic scheme for the polymer C0 is shown in Scheme S1. BDSA includes around 30% water as received so it was washed with acetone before use. 5.0 g of BDSA was dispersed in 200 mL of acetone, and it was stirred for 2 hours. After that, the solid was collected by filtration, then dried at 70 °C overnight to obtain the dehydrated BDSA with 97% yield. Other reagents were purchased with high purity from commercial suppliers and used without further purification. 0.13 g NTDA (0.50 mmol) and 0.17 g BDSA (0.50 mmol) were put into a three-necked flask. Since BDSA was highly hygroscopic, it was weighed and purged into the flask as soon as possible. Then 5 mL of *m*-cresol and 150 μL (1.1 mmol) of triethylamine (TEA) were added and stirred under an

Ar atmosphere at room temperature to neutralize the sulfonic acid groups in BDSA. The mixture was heated to 170 °C for 6 hours under stirring to synthesize C0. After the reaction, the reaction liquid was poured into 200 mL of ice-cold acetone to precipitate polymers, then the polymer was collected by centrifugation at 7500 rpm for 3 minutes. The solid was further washed with ice-cold acetone 3 times with the same centrifugation condition, then dried in a desiccator. The obtained polymer was dissolved in 250 mL pure water under stirring at room temperature, and subjected to ion exchange using the cation exchange resin Amberlite 31WET (Organo) to yield protonated C0. The amount of resin was adjusted so that the ion exchange capacity was four times greater than the amount of sulfonic acid groups in the polymer. The solution was passed through the resin five times to ensure complete ion exchange. The polymer solution after the ion exchange was dried using a rotary evaporator (Yamato Scientific), then dissolved in a small amount of water (~20 mL) and vacuum-dried overnight in a vacuum specimen dryer VSD-95 (Ishii Shoten). The product yield from the monomer was 60%. The degree of protonation, determined from the integral ratio of the TEA peak in the ¹H nuclear magnetic resonance (NMR) spectrum, was 98%. NMR spectrum is shown in Figure S1. IR (cm⁻¹): 1710 ($v_{C=O}$, sym), 1667 ($v_{C=O}$, asym), 1581 ($v_{C=C}$), 1468 ($v_{C=C}$), $1350 (v_{C-N})$, $1251 (v_{S=O}, asym)$, $1200 (v_{S=O}, sym)$, $1028 (v_{S=O}(SO^{-}), asym)$. Sym and asym denote the symmetric and asymmetric modes, respectively. The weight-average molecular weight $(M_{\rm w})$ and polymer dispersity of C0 were 3.5×10^5 and 5.5, respectively.

2.2.2. Synthesis of C6

3,3'-Bis(6-sulfohexyloxy)benzidine (BSHB), essential for the synthesis of **C6**, was newly synthesized. The synthetic scheme of BSHB is illustrated in Schemes S2a to S2f, and the details for BSHB synthesis is provided in Figures S2 and S3, Supporting Information.

The synthetic scheme for the polymer C6 is shown in Scheme S3. In a three-neck flask, 0.27 g (0.50 mmol) of BSHB and 0.13 g (0.50 mmol) of NTDA were added, and the flask was equipped with a condenser and purged with Ar gas. Then, 5 mL of m-cresol and 150 μL (1.1 mmol) of TEA were added to neutralize the sulfonic acid groups in BSHB, and the mixture was refluxed with stirring at 150 °C for 6 hours to synthesize the polymer. After the reaction, the reaction liquid was poured into 200 mL of ice-cold acetone to precipitate polymers, then the polymer was collected by centrifugation at 7500 rpm for 3 minutes. The solid was further washed with ice-cold acetone 3 times with the same centrifugation condition, then dried in a desiccator. The obtained polymer was dissolved in 400 mL pure water under stirring at room temperature, and subjected to ion exchange using the cation exchange resin Amberlite 31WET (Organo) to obtain C6. The amount of resin was adjusted to achieve an ion exchange capacity four times greater than that of the sulfonic acid groups in the polymer. The solution was passed through the resin five times to ensure complete ion exchange. The ion-exchanged solution was dried using a rotary evaporator and then dissolved in a small amount of water (~20 mL) and vacuum-dried overnight in a vacuum specimen dryer. The yield from the monomer was 62%, and the degree of protonation determined from the ¹H NMR spectrum as shown in Figure S1 was 97%. IR (cm⁻¹): 2940 (ν_{C-H} (CH₂), asym), 2859 (ν_{C-H} _H (CH₂), sym), 1713 ($\nu_{C=O}$, sym), 1670 ($\nu_{C=O}$, asym), 1580 ($\nu_{C=C}$), 1468 (δ_{C-H} (CH₂), asym), 1451 $(v_{C=C})$, 1349 (v_{C-N}) , 1249 $(v_{S=O}, asym)$, 1198 $(v_{S=O}, sym)$, 1035 $(v_{S=O}(SO^-), asym)$. The peaks from the amide group and carbonyl group were not observed, suggesting that imidization was completed. The $M_{\rm w}$ and polymer dispersity of C6 were 3.6 \times 10⁵ and 3.9, respectively.

2.2.3. Synthesis of C10

The diamine monomer 3,3'-bis(10-sulfodecyloxy)benzidine (BSDB) was synthesized partly following the previous report by Yasuda and Miyatake *et al.*²⁴⁻²⁵ The details for BSDB monomer synthesis are shown in Schemes S4a to S4d and Figure S4 in Supporting Information.

The synthetic scheme for the polymer C10 is shown in Scheme S5. In a three-neck flask, 0.33 g (0.50 mmol) of BSDB and 0.13 g (0.50 mmol) of NTDA were added, and the flask was equipped with a condenser and purged with Ar gas. Then, 5 mL of m-cresol and 150 μL (1.1 mmol) of TEA were added to neutralize the sulfonic acid groups in BSDB, and the mixture was refluxed with stirring at 150 °C for 6 hours under stirring to synthesize the polymer. After the reaction, the reaction liquid was poured into 200 mL of ice-cold acetone to precipitate polymers, then the polymer was collected by centrifugation at 7500 rpm for 3 minutes. The solid was further washed with ice-cold acetone 3 times with the same centrifugation condition, then dried in a desiccator. The resulting polymer was insoluble in deionized water, hence ion exchange was performed using a hydrochloric acid solution. Specifically, the sample was immersed in a 200 mL of 1 mol L^{-1} hydrochloric acid solution in ethanol for 12 hours, the solid was collected by centrifugation at 7500 rpm for 3 minutes. The solid was dispersed in 100 mL ethanol, and collected by centrifugation with the same centrifugation condition. This process was repeated three times. The progress of the ion exchange was confirmed by the disappearance of the TEA peak in the ¹H NMR spectrum. After that, the solid was washed with 40 mL ethanol 4 times to completely remove hydrochloric acid. Finally, the sample was vacuum-dried at 50 °C to obtain C10. The yield from the monomer was 83%. As shown in Figure S1, the absence of residual TEA peaks in the ¹H NMR spectrum indicates that protonation was almost complete. IR (cm⁻¹): 2925 (v_{C-H} (CH₂), asym), 2853 (v_{C-H} (CH₂), sym), 1715 ($\nu_{C=O}$, sym), 1672 ($\nu_{C=O}$, asym), 1580 ($\nu_{C=C}$), 1467 (δ_{C-H} (CH₂), asym), 1448 $(v_{C=C})$, 1347 (v_{C-N}) , 1248 $(v_{S=O}$, asym), 1196 $(v_{S=O}$, sym), 1032 $(v_{S=O}(SO^-)$, asym). It should be noted that the peak positions of asymmetric v_{C-H} (CH₂) at 2925 cm⁻¹, symmetric v_{C-H} (CH₂) at 2853 cm⁻¹, and asymmetric δ_{C-H} (CH₂) at 1467 cm⁻¹ are consistent with those of straight-chain hydrocarbon dodecane (asymmetric v_{C-H} (CH₂) at 2926 cm⁻¹, symmetric v_{C-H} (CH₂) at 2953 cm⁻¹ and asymmetric δ_{C-H} (CH₂) at 1464 cm⁻¹). This indicates that the carbon atoms at side-chain dominantly aligned in trans conformation. The M_w and polymer dispersity of C10 were 1.4 × 10⁵ and 3.5, respectively. Toward the fuel cell application, the chemical stability of C10 membrane was examined. We investigated the Fenton's test by immersing the ~100 μ m C10 membrane in freshly prepared 3% H₂O₂ aqueous solution containing 2 ppm Fe²⁺ ions at 80 °C for 1 hour (See Supporting Information for details). We found that the C10 membrane retained its morphology and weight after the Fenton's test. Moreover, little decrease of molecular weight was detected, and trace of removal of the side chain group or the imide ring-opening was not observed from ¹H NMR (Figure S5) and attenuated total reflectance-IR (ATR-IR, Figure S6) spectra.

2.3. Characterization of SPIs

2.3.1. ¹H Nuclear Magnetic Resonance (¹H NMR) Spectroscopy

Obtained monomers and polyimides were identified using ¹H NMR spectra. The measurements were performed using an AVANCE III 400 MHz (Bruker) spectrometer. The measurement solutions were prepared by dissolving the monomers and polyimides in deuterated dimethyl sulfoxide (DMSO-*d*₆) containing 0.03% trimethylsilane as an internal reference. A volume of 500 µL of the prepared solution was taken in an NMR sample tube. The identification of peaks and the calculation of integration values were performed using the 1D NMR analysis software.

2.3.2. Fourier Transform Infrared Spectroscopy with Attenuated Total Reflectance (FTIR ATR)

The synthesized polyimides were identified using Fourier transform infrared spectroscopy with attenuated total reflectance (FTIR ATR). The measurements were carried out using a Nicolet 6700 (Thermo Fisher Scientific) spectrometer, and OMNIC software (Thermo Fisher Scientific) was used for analysis. The ZnSe prism was cleaned with ethanol, and a background measurement was performed without the sample. After the background measurement, each SPI powder was placed on the prism to cover it, and the powder was pressed onto the prism using a compression device before measurement. Both background and sample measurements were performed with 32 scans. The obtained spectra were corrected for distortion using the Advanced ATR Correction feature in OMNIC.

2.3.3. Gel Permeation Chromatography (GPC)

The molecular weights of the synthesized polyimides were measured using gel permeation chromatography (GPC). The measurements were performed using an LC-2000plus (JASCO Corporation) instrument. The GPC eluent was prepared by dissolving 10.26 g of NaNO₃ in 600 mL of distilled water and 400 mL of N,N'-dimethylformamide, followed by the addition of 18 mL of acetic acid. The molecular weights were calculated by comparison with a standard calibration curve. The standard calibration curve was created by measuring standard polystyrene samples with known molecular weights ($M_w = 759000, 126700, 16000, 1690$) dissolved in the mobile phase solution at 5 wt%.

For C10, which was insoluble in the above eluent, the eluent of N,N'-dimethylformamide with 0.01 M LiBr was used and the measurements were performed using a KD-806M column (Shoko Science Co., Ltd.). Standard polyethylene glycol samples with known molecular weights ($M_{\rm w} = 759000, 580000, 290000, 101000, 23600$) were used to create the standard calibration curve.

2.4. Preparation of Thin Films by Spin Coating

Thin films used for structural and orientation evaluation, water molecule adsorption, and proton conductivity measurements were prepared by spin coating. Each SPI was dissolved in a mixed solvent of deionized water: tetrahydrofuran (THF) = 1: 1. The spin coating was performed using an Active Spin Coater ACT-220D (Active). Concentration of the solution was optimized to obtain approximately 500 nm film thickness. For orientation evaluation, a high-resistance Si wafer (Electronics and Materials Corporation) was used as the substrate, and for proton conductivity measurements, SiO₂ was used as the substrate. As a pretreatment, the substrates were immersed in 2-propanol and subjected to ultrasonic treatment for about 30 minutes. Immediately before thin film fabrication, the substrates were plasma-treated using a plasma apparatus Cute (FEMTO SCIENCE) to remove adhered organic compounds and improve the wettability of the substrate surface. The thickness of the films was evaluated using a white light interferometer (WIM) and an atomic force microscope (AFM). For the thin films deposited on SiO₂ substrates, the films were scratched in a grid pattern using a cotton swab moistened with a water/THF mixed solution, and the thickness was determined by averaging the thicknesses measured at four edges using WIM. Similarly, for the thin films deposited on Si substrates, the films were scratched in a cross pattern using a cotton swab moistened with a water/THF mixed solution, and the thickness was determined by averaging the thicknesses measured at four arbitrary points using AFM.

2.5. Polarizing Optical Microscopy (POM)

The internal structure of each polyimide thin film was evaluated using polarizing optical microscopy (POM). The measurements were performed using a BX51-P (Olympus) microscope and a DP28 camera (Olympus). The data were recorded using CellSens Controller software.

2.6. Infrared p-Polarized Multiple Angle Incidence Resolution Spectrometry (IR pMAIRS)

The molecular orientation of the thin films was measured using p-polarized multiple-angle incidence resolution spectrometry (IR pMAIRS). IR pMAIRS is a type of infrared spectroscopy that simultaneously acquires spectra in the IP direction, parallel to the substrate, and the out-of-plane (OP) direction, perpendicular to the substrate.²³ Measurements were performed on films deposited on high-resistance Si substrates using a Nicolet 6700 (Thermo Fisher Scientific) spectrometer, and pMAIRS software (Thermo Fisher Scientific). To avoid interference from water vapor peaks, the instrument was thoroughly purged with dry air or dry N₂ before measurement. The incident angle of the substrate was varied from 38 to 8° in 6° increments, making six observations. The vertical axis to the substrate is defined as 0°. Spectra at each angle were accumulated 64 times. A background spectrum was first recorded with the Si substrate alone, followed by measurement of the substrate with the deposited film. The average orientation angle can be determined using the following equation:

$$\phi = \tan^{-1} \sqrt{\frac{2A_{\rm IP}}{n^4 H A_{\rm OP}}}, (1)$$

Where $A_{\rm IP}$ and $A_{\rm OP}$ represent the absorbance of each band in the IP and OP spectra, respectively, and ϕ is the orientation angle from the substrate's vertical direction. As correction factors, n is the refractive index of SPI, taken as 1.6, and H is the substrate correction factor, taken as 0.13.

2.7. In situ Quartz Crystal Microbalance (QCM) Measurement under Controlled Humidity

The water molecule adsorption of each SPI thin film was determined using a homemade in situ quartz crystal microbalance (QCM) system. The RH was controlled using a humidity generator (Bel Flow, Nippon Bell) by mixing appropriate amounts of dry nitrogen and humid nitrogen. The

QCM substrate was connected to an oscillation circuit and a frequency counter (5313A, Agilent Technologies) and set in a custom-built humidity chamber equipped with a high-resolution RH sensor (TR-72wf, T&D Corporation). The weight change Δm of the thin film was determined using Sauerbrey's equation:

$$\Delta m = \frac{S \times \sqrt{\rho \mu}}{2 \times F^2} \times (-\Delta F), (2)$$

where S represents the electrode surface area, ρ and μ denote the quartz density and quartz shear modulus, and F stands for the fundamental frequency of the QCM substrate. The water molecule adsorption amount per sulfonic acid group, λ , was determined using the following equation:

$$\lambda = \left(\frac{m}{m_0} - 1\right) \times \frac{EW}{M_{\rm H_2O}}, (3)$$

where m signifies the film mass at each RH, m_0 stands for the film mass at the 0% RH, $M_{\rm H2O}$ denotes the molecular mass of water molecular, and EW expresses the equivalent weight of each SPI. The EW values for each SPI are as follows: **C0** is 289 g eq⁻¹, **C3** is 346 g eq⁻¹, **C6** is 389 g eq⁻¹, and **C10** is 445 g eq⁻¹.

2.8. In situ Grazing Incidence X-ray Scattering (GIXRS) Measurement under Controlled Humidity

The structural changes in each SPI thin film during humidification were measured using in situ grazing incidence X-ray scattering (GIXRS) under controlled humidity. An ultra-bright X-ray generator FR-E (RIGAKU) was used with a Cu *Kα* X-ray source. The collimated X-ray beam (approximately 300 μm in diameter) was directed at the sample, and the diffraction was detected using an imaging plate X-ray detector R-AXIS IV (RIGAKU). The substrate samples were placed

on a grazing incidence measurement stage (tilting stage ATS-C316-EM / Z-axis stage ALV-300-HM, Chuo Precision Industrial Co., Ltd.) and irradiated with X-rays at an incident angle of approximately 0.2°. The camera length was set to 300 mm, and the direct beam was blocked by a beam stopper. The RH inside the Kapton film cell was controlled by a vapor generator BELFlow (Nippon Bell) and measurements were taken at 0 - 95% RH at room temperature.

2.9. Alternating Current (AC) Impedance Measurements

The IP proton conductivity of SPI thin films was measured using the alternating current (AC) impedance method. The thin films, cut into squares of approximately 5 mm on each side, had gold paste applied to both ends, with gold wires attached to serve as electrodes. The impedance of the thin films was measured using a 1260 Impedance/gain-phase analyzer (Solartron Analytical), an amplifier 1296 Dielectric interface (Solartron Analytical), and a constant temperature and humidity chamber SH-221 (Espec Corp.). An AC voltage of 50 mV was applied, and the impedance was measured while scanning frequencies from 1 Hz to 10 MHz. Measurements were taken at a temperature of 25 °C and humidity ranging from 40% to 95% RH or at a humidity of 90% RH and temperature ranging from 20 to 80 °C. Proton conductivity (σ) was calculated using the following equation:

$$\sigma = \frac{d}{Rlt}, (4)$$

where d is the distance between electrodes, R is the resistance obtained from the AC impedance measurement, l is the electrode length, and t is the film thickness, respectively. The activation energy (E_a) of the proton conduction was calculated according to the Arrhenius equation as following equation (5):

$$\sigma T = \sigma_0 \exp(-\frac{E_a}{RT}), (5)$$

therein, R, T, and σ_0 respectively represent the gas constant, temperature and pre-exponential factor, respectively.

2.10. In situ FTIR Measurement under Controlled Humidity

The adsorption process of water molecules and the acid dissociation state of sulfonic acid groups were analyzed using in situ FTIR under controlled humidity. The same measurement apparatus as described in Section 2.3.2 was used. A transmission cell with CaF₂ windows was constructed, and the RH inside the cell was controlled using a precise small-scale humidity generator me-40DP-2PW (Micro equipment). Measurements were conducted at 0 - 95% RH.

2.11. Computational Screening for Stable Conformations

The SMILES codes of C0, C3, C6 and C10 polymer units were used to create the 3D polymer unit coordinates of 100 different molecular conformations using the experimental-torsion-knowledge distance geometry (ETKDG) version 3 method²⁶⁻²⁸ implemented in the Python library RDKit.²⁹ The potential energy of each conformation of polymer unit was evaluated by the universal neural network potential (UNNP) called PreFerred Potential (PFP) version 4.0^{30} including dispersion correction (D3)³¹⁻³² using the Matlantis software package.³³ The geometry optimization of each conformer was carried out by the limited-memory Broyden-Fletcher-Goldfarb-Shanno (L-BFGS) algorithm with $f_{\text{max}} = 0.01$ convergence criteria. All the conformers relative potential energy to each other were determined and used to calculate Boltzmann distribution. The preferable conformations were visualized using Ovito software.³⁴

3. Results and Discussion

3.1 POM Observations

Previous studies have shown that alkyl-sulfonated polyimide thin films exhibit an organized structure with LC domains visible under POM.²¹ To investigate the effect of different alkyl side chain lengths, POM observations were performed on the synthesized SPI thin films. Figure 2 shows the POM images of C0 (Figures 2a and 2b), C3 (Figures 2c and 2d), C6 (Figures 2e and 2f), and C10 (Figures 2g and 2h) thin films, respectively. Birefringence was observed in all SPI thin films, with domains approximately 100 μm in diameter detected in each sample. While C3 thin film has been previously reported to exhibit birefringence,²¹ this study confirms that altering the carbon number in the alkyl side chain also results in birefringence across all samples, confirming the LC properties in all SPI thin films. Additionally, the shape of the LC domains varied with the carbon number of the alkyl side chain, indicating that the side chain length influences the morphology of these domains.

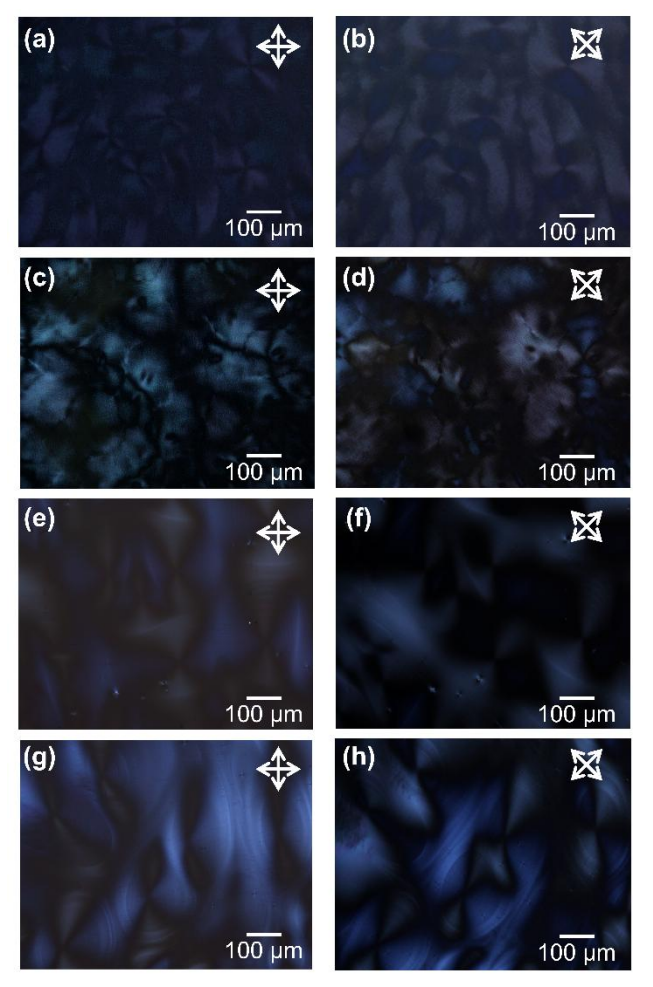


Figure 2. POM images of (a and b) **C0**, (c and d) **C3**, (e and f) **C6**, and (g and h) **C10** thin films at 0 and 45°, respectively.

3.2 IR pMAIRS Results for Backbone Orientation

Aromatic polyimides are known for their rigid and planar structures, which typically result in the polymer backbone aligning parallel to the substrate when cast as thin films.³⁵ This alignment has been previously observed in C3 thin films.¹³ To investigate the alignment of the other SPI thin films, we performed IR pMAIRS measurements of approximately 500 nm thickness SPI thin films on Si substrates, as shown in Figure 3. For all polymers, peaks corresponding to the symmetric

stretching vibration $v_{\text{sym}}(C=O)$ and asymmetric stretching vibration $v_{\text{asym}}(C=O)$ of the imide ring were observed at 1720 cm⁻¹ and 1680 cm⁻¹, respectively. Additionally, the stretching vibration ν (C-N) of the C-N-C linkage along with the main chain direction appeared at 1350 cm⁻¹. Peaks at 1250 cm⁻¹ and 1190 cm⁻¹ were attributed to the asymmetric v_{asym}(S=O) and symmetric $v_{\text{sym}}(S=O)$ stretching vibrations of the sulfonate groups, respectively. The peak at 1030 cm⁻¹ was assigned to the asymmetric stretching vibration $v_{asym}(S=O)$ of the dissociated sulfonate groups (SO₃⁻). For polyimide thin films with alkyl chains, the bending vibration $\delta_{asym}(C-H)$ of the methylene groups was observed at 1470 cm⁻¹. The significant difference between the IP and OP absorbance in the IR pMAIRS measurements reflects the anisotropic orientation of the molecular structure. All thin films exhibited stronger IP absorbance than OP absorbance for the C=O symmetric and C-N stretching vibration modes, indicating that the polymer backbones were oriented parallel to the substrate. The average orientational angle of the polymer backbones estimated from equation (1) and C-N stretching vibration mode for C0, C3, C6, and C10 thin films was 61, 60, 62, and 63°, respectively. These results suggest that the backbone alignment is consistent regardless of the alkyl side chain length.

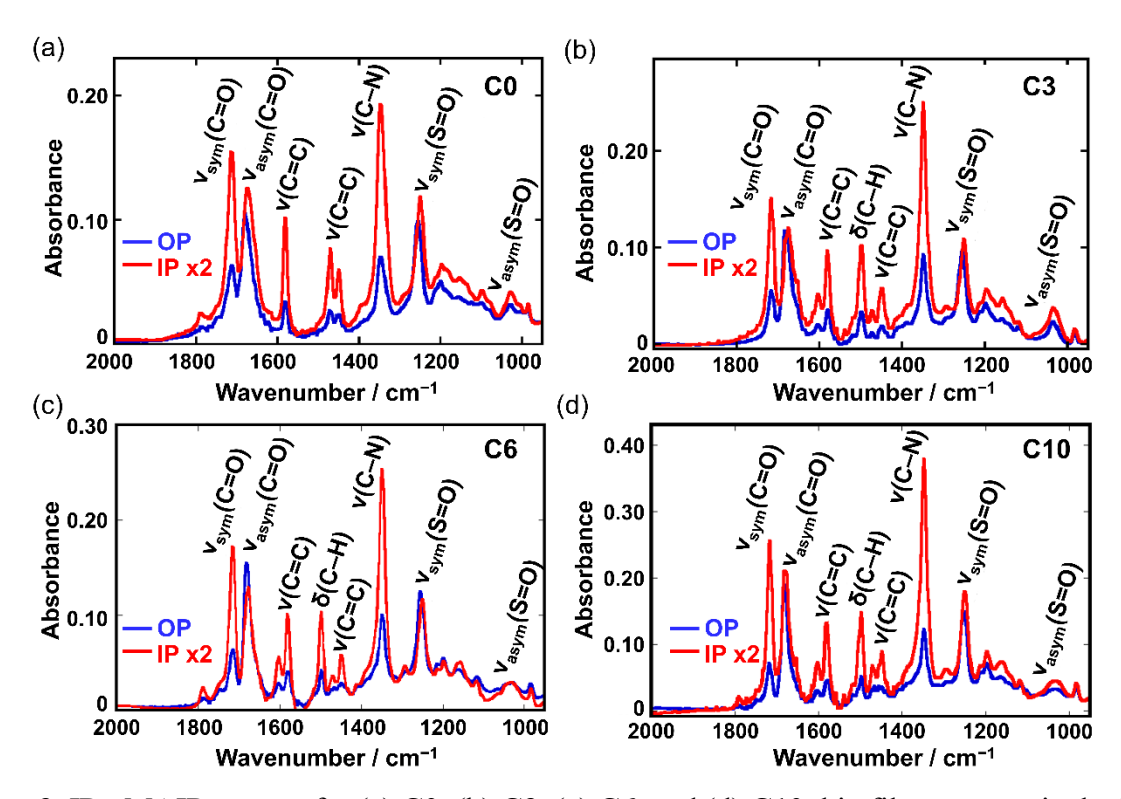


Figure 3. IR pMAIR spectra for (a) **C0**, (b) **C3**, (c) **C6**, and (d) **C10** thin films, respectively. IP x2 corresponds to twice-multiplied IP absorbance for clear discussion of the orientation angle.

3.3 Water Uptake by QCM

The number of absorbed water molecules is a crucial parameter in considering lyotropic LC properties. To quantitatively discuss the water uptake, in situ QCM measurements were conducted under controlled humidity. Figure 4 shows the RH-dependent water uptake per -SO₃H group λ of the SPI thin films at 25 °C, calculated from equations (2) and (3). The water adsorption isotherms exhibited behavior similar to that of non-porous multilayer adsorption isotherms, indicating a transition from monolayer to multilayer water adsorption. The **C0** thin film demonstrated the highest water uptake in the 20 - 70% RH range, and at > 80% RH regions the uptake was consistent with **C3** and **C6**. The **C10** thin film exhibited the lowest water uptake among four SPI thin films

in the whole RH region, and this tendency was remarkable under high humidity conditions. This lower water uptake is attributed to the lower hydrophilicity of C10, as evidenced by its insolubility in water.

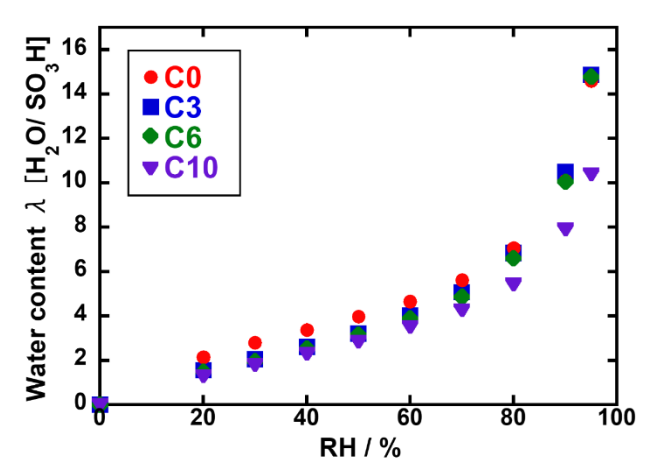


Figure 4. RH-dependent water uptake plots for C0, C3, C6 and C10 thin films.

3.4 Structural Analysis Using GIXRS: Effects of Humidity and Side Chain Length on Lamellar Spacing

To investigate the internal structures, in situ GIXRS measurements were conducted under controlled humidity conditions. Figure 5 presents the 2D GIXRS images at 50% and 95% RH (See also Figures S7 to S10), and their 1D profiles for both IP and OP directions for each SPI thin film. Table 1 summarizes the d spacing and assignment in the IP and OP directions. For comparison, previously reported data for C3 thin film were also shown in Figure 5(b).²¹ The C3 thin film has been reported to form a lamellar structure due to its lyotropic LC properties. In Figure 5(b), a scattering peak in the OP direction at $\alpha = 3.1 - 6.8^{\circ}$ corresponds to the lamellar spacing. This scattering peak increased in intensity and shifted to lower angles with increasing humidity,

indicating enhanced regularity, and expanded spacing of the lamellar structure due to water uptake. In the IP direction, a scattering peak corresponding to the polymer unit length (d = 1.6 - 1.7 nm) was observed.

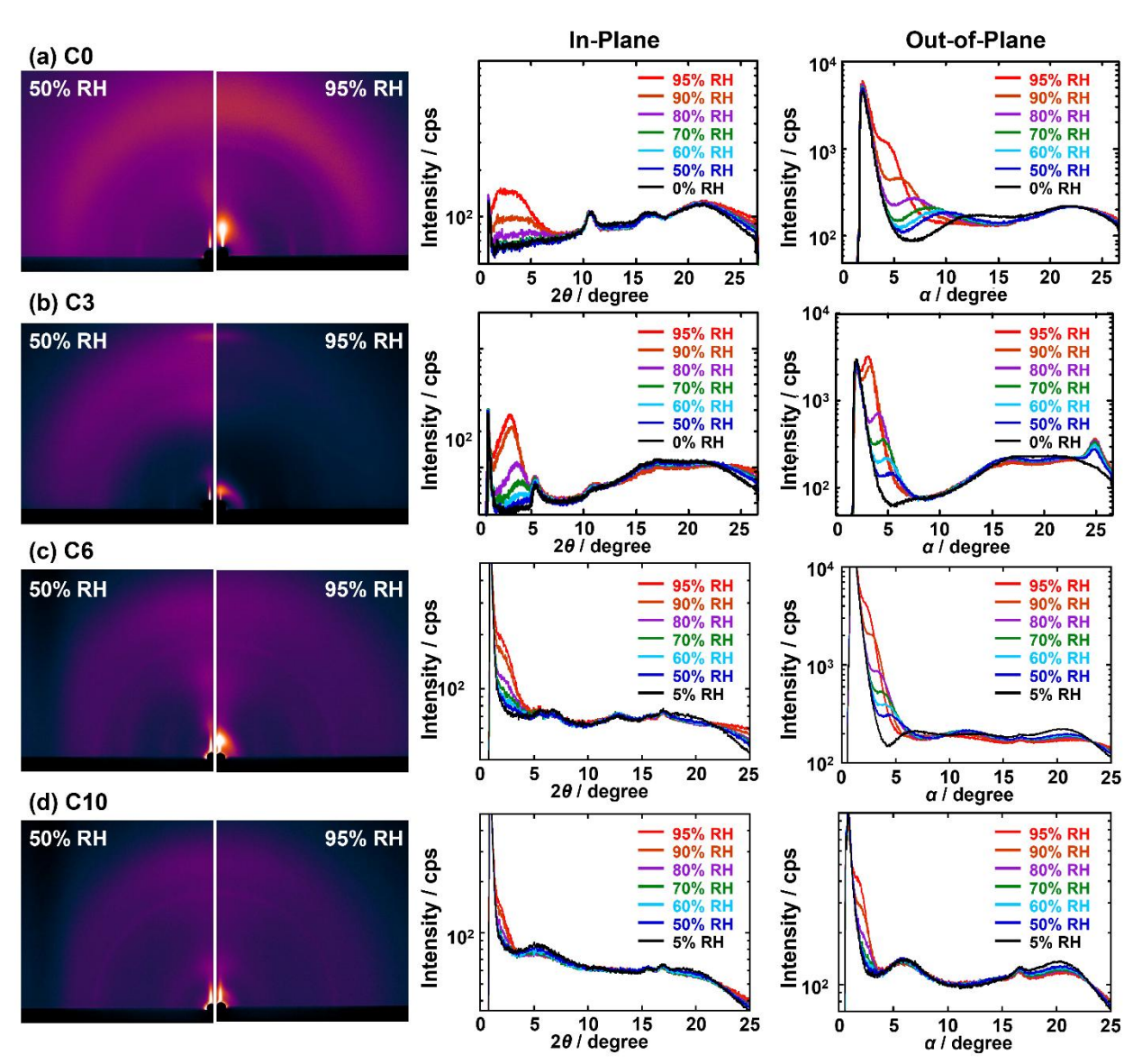


Figure 5. RH-dependent 2D GIXRS images of (a) **C0**, (b) **C3**, (c) **C6**, and (d) **C10** thin films at 50% (left) and 95% RH conditions (right). The horizontal and vertical directions correspond to the IP and OP directions, respectively. Also, their projected 1D profiles in the IP and OP directions at

each RH were shown at the right side of each 2D images, respectively. 2θ and α correspond to the scattering angles in IP and OP directions, respectively.

Table 1. d spacing and assignment in the IP and OP directions of SPI thin films

d spacing / nm				
Thin film	direction	0% RH	95% RH	assignment
C0	OP	0.67	2.2	lamellar
	IP	0.83	0.83	secondary scattering of the polymer unit length
С3	OP	1.3	2.9	lamellar
	IP	1.6	1.6	polymer unit length
C6	OP	1.4	4.0	lamellar
	IP	1.6	1.6	polymer unit length
C10	OP	-	5.1	lamellar
	IP	1.7	1.7	polymer unit length (broad)

Figure 5(a) showed a scattering peak at $\alpha = 4.0$ - 13.2° in the OP direction for the **C0** thin film, indicating the formation of a lamellar structure. The lamellar spacing increased from 0.67 nm at 0% RH to 2.2 nm at 95% RH, which was narrower compared to the **C3** thin film due to the absence of the side chains. Moreover, in the IP direction, the secondary scattering of the polymer unit length was observed at 0.83 nm. This assignment was further verified from the GIXRS measurement of the shear-oriented **C0** thin film (Figures S11 and S12 in Supporting Information). Figure 5(c) showed that **C6** thin film exhibited a scattering peak at $\alpha = 2.2$ - 6.3° in the OP direction, with the lamellar spacing increasing from 1.4 nm at 5% RH to 4.0 nm at 95% RH, indicating wider spacing compared to the **C3** thin film. Figure 5(d) showed that the **C10** thin film did not exhibit a lamellar scattering peak from 5% to 50% RH. However, at RH $\geq 60\%$, a scattering peak in the OP direction corresponding to the lamellar structure was observed, suggesting that the **C10** thin film formed a more ordered structure with increasing humidity. The lamellar spacing reached 5.1 nm

at 95% RH, which was further wider than that of the **C6** thin film. It is to be noted that the lamellar spacing at 95% RH in **C10** was the largest among reported the SPI thin film. 17-21

These findings indicate that all SPI thin films form lyotropic lamellar structures upon hydration, with lamellar spacing increasing with longer alkyl side chains. Figure 6(a) presents a schematic illustration of the proposed lamellar structures of each SPI thin film at 95% RH. Figure S13 plots the lamellar spacing against the carbon number of the alkyl side chains at 95% RH, showing a nearly linear relationship. This result demonstrates that the lamellar spacing in SPI thin films can be controlled by the length of the alkyl side chains. Figure S14 plots the lamellar spacing against the water uptake λ obtained from in situ QCM measurements, showing that the lamellar spacing increases linearly with water uptake. Figure 6(b) plots the lamellar spacing at $\lambda = 10$ for each SPI thin film, showing a nearly linear relationship to the number of carbon atoms at $\lambda = 10$.

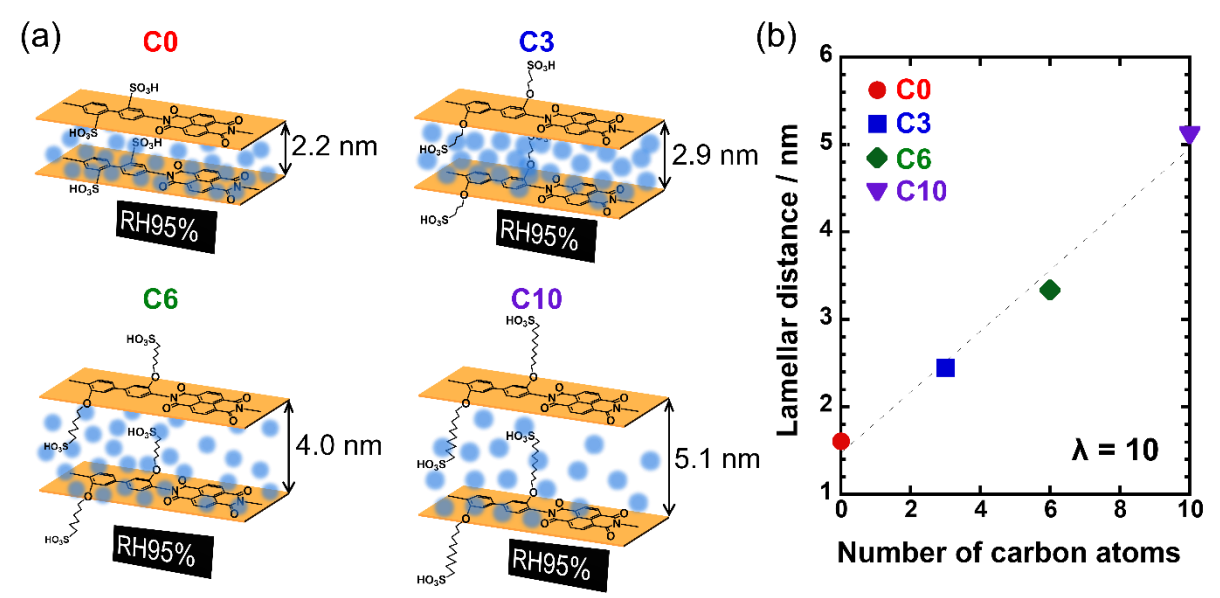


Figure 6. (a) Schematic illustration of the proposed lamellar structures of each SPI thin film at 95% RH. Orange plates correspond to the polyimide backbone planes. Light blue balls represent the absorbed water molecules, whose amount was varied based on the experimental water uptake

amount from QCM measurement. (b) Relationship between the number of carbon atoms at the side chain and lamellar distance at the water content of $\lambda = 10$.

3.5 Impact of Side Chain Length on Proton Conductivity and Proton Dissociation

The RH-dependent proton conductivity of C0, C3, C6, and C10 thin films parallel to the organized lamellar structure is shown in Figure 7(a), as calculated from equation (4). The logarithm of the proton conductivity exhibited a linear increase with RH. At 95% RH and 25 °C, the proton conductivities were $7.5 \times 10^{-2} \text{ S cm}^{-1}$ for the **C0** thin film, $9.6 \times 10^{-2} \text{ S cm}^{-1}$ for the **C6** thin film, and 3.4×10^{-2} S cm⁻¹ for the C10 thin film. These values are higher than that of Nafion thin film with similar thickness at 298 K and 95% RH,²⁰ and comparable to SPIs with bent and aromatic dianhydride backbones among the reported SPIs.²¹ It has been reported that C3 thin film demonstrated a proton conductivity of 1.8 × 10⁻¹ S cm⁻¹ at 95% RH and 25°C. ¹³ These results indicated that SPI thin films with an alkyl side chain length of three carbon atoms exhibited highest proton conductivity under > 70% RH, while at low RH regions, the conductivity was highest in SPI without an alkyl chain. Additionally, as the alkyl side chain length increased from three carbon atoms, the conductivity decreased. Since the influence of water molecule adsorption on proton conductivity is significant and water molecules facilitate the proton transport, the proton conductivities were plotted against the water uptake λ (Figure 7(b)). All thin films exhibited an increase in conductivity with an increase of λ , reaching maximum conductivity at maximum water uptake. When comparing proton conductivities at the same water uptake levels, the C3 thin film displayed highest proton conductivity at water uptake levels above $\lambda \approx 5$. The proton conductivity of the C0 thin film was highest around $\lambda = 3.5$. This is attributed to the lower p K_a value of the proton in this SPI compared to the other SPIs, facilitating easier proton dissociation and transport. On the other hand, at 95% RH, C3 thin film showed a higher scattering intensity and smaller full

width at half-maximum than C0 thin film (C0: 0.99°, C3: 0.84°) of lamellar scattering from the GIXRS (Figure 4). This result indicates that C3 exhibits a more ordered organized structure than C0, possibly one factor for higher proton conductivity in C3 thin film than C0 thin film at high RH.

To get insight into the conduction mechanism, the temperature dependence of proton conductivity was investigated in the temperature range of 20-80 °C at a constant RH of 90% (Figure S15). In cases of the C0 thin film, proton conductivity could not be measured due to the dissolution of the thin film by humidification at high temperatures. The estimated activation energies (E_a in equation (5)) for proton conduction of C6 and C10 thin films are 0.21 eV and 0.25 eV, respectively. It has been reported that the E_a of the C3 thin film was 0.18 eV.²¹ These results indicate that the activation energy increases with the length of the side chain. Comparing C3, C6 and C10, the longer lamellar distance was revealed at 95% RH as the alkyl side chain length increased (Table 1), while the water uptake of C3 thin film was comparable to that of C6 thin film and higher than that of C10 thin film at 95% RH (Figure 4). These indicate the decrease in density of water in the lamellar structure at longer side chain length. Moreover, from GIXRS scattering at 95% RH, the peak width of lamellar scattering in the OP direction increased as the side chain length elongated (C3: 0.84°, C6: 0.91°, C10: 0.93°). Also, the scattering assignable to the monomer unit length in IP profiles was more intense and sharper in C3 compared with C6 and C10. These were possibly derived from the enhanced alkyl side chain motion at longer side chain length. These results indicate the longer-range ordering of the organized structure in C3 than in C6 and C10 at high RH. These resulted in the formation of a less smooth proton conduction pathway, higher E_a and lower proton conductivity as the side chain length X increases.

To gain further insights into water molecule adsorption, RH in situ FTIR measurements were conducted to analyze the adsorption process under controlled humidity. Figures S16-S19 show the results for SPI thin films in the whole regions, and Figures 7(c) to (f) shows the same spectrum in the range of 950 - 1850 cm⁻¹ for discussing the proton dissociation state, *vide infra*. In all materials, a broad absorption band attributed to the OH stretching vibration of water molecules appeared at 3420 cm⁻¹, increasing in absorbance with humidity. This frequency is consistent with that of bulk water.³⁶⁻³⁷

The RH-dependent deprotonation of the sulfonic acid groups was also analyzed. In Figures 7(c) to (f), the absorption attributed to the asymmetric stretching vibration v_{asym} (S=O) of dissociated sulfonic acid groups (SO₃⁻) was observed at 1030-1040 cm⁻¹ in all spectra.³⁸⁻³⁹ The rate of proton dissociation (PD) from sulfonic acid groups at different RH levels was calculated using the following formula:

PD =
$$\frac{S_{x(SO_3^-)} - S_{0(SO_3^-)}}{S_{95(SO_3^-)} - S_{0(SO_3^-)}} \times 100$$
, (6)

where $S_{x(SO3^-)}$ corresponds to the peak area of $v_{asym}(S=O)$ at x% RH. Figures S20-23 show PD plots against RH from formula (6). The increasing trend of proton dissociation from sulfonic acid groups varied among the different polyimide thin films with RH.

The C0 thin film showed the most steep increase of PD at low RH among the four SPIs (~75% PD at 40% RH), while the other SPI thin films with alkyl side chains showed up to 60% PD at 40% RH. The higher acidity (lower p K_a) of C0 (p $K_a = -2.5$) compared to C3 (p $K_a = -0.6$)⁴⁰ explains the differences in proton dissociation trends. The proton dissociation trend, which differs due to the presence or absence of alkyl side chains, significantly impacts proton conductivity.

Proton conduction occurs through vehicle mechanisms and the Grotthuss mechanism involving protons dissociated from sulfonic acid groups. Thus, the higher proton dissociation rate of **C0** at up to 40% RH contributes to the higher proton conductivity. Clear differences in proton dissociation trends were not observed among polyimides with different alkyl side chain lengths.

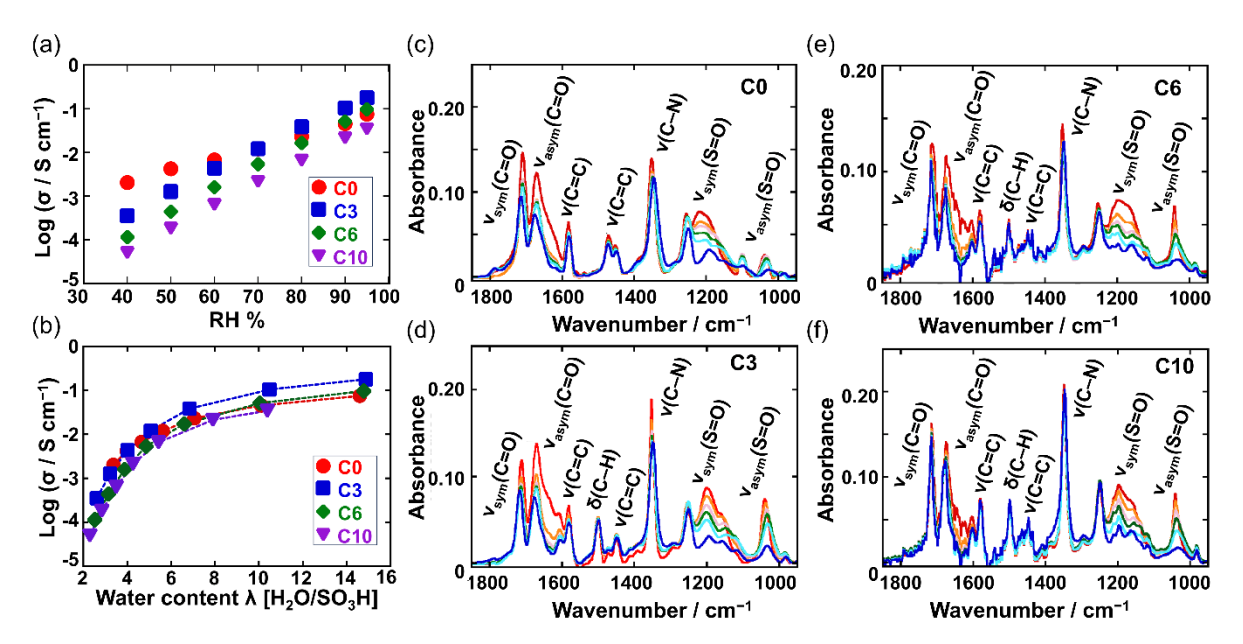


Figure 7. (a) and (b) Proton conductivity for C0, C3, C6, and C10 thin films as a function of (a) RH and (b) water uptake λ . (c) to (f) RH-dependent in situ FTIR spectra in the wavenumber region between 950 - 1850 cm⁻¹ for (c) C0, (d) C3, (e) C6, and (f) C10 thin films. Blue, right blue, green, pink, orange and red lines correspond to the spectra measured at 0%, 20%, 40%, 60%, 80% and 95% RH, respectively.

3.7 Computational Analysis of Alkyl Side Chain Length Impact on Proton Conductivity

The computational conformation analysis allowed us to elucidate the effect of the alkyl side chain length on proton conductivity. The potential energy landscape of conformations (> 1% probability

distribution) in each SPI units without water molecules is shown in Figure S24. C3, C6 and C10 had one stable conformation as shown in Figure 8, and the interaction between the adjacent sulfonic acid groups or sulfonic acids group and the polymer backbone was observed. On the other hand, there is no clear energy difference among the conformers in C0 due to the absence of such interactions. The structural difference between the most stable conformation in Figure 8 and the conformations close to it is just the small change in the rotation angle of sulfonic acid groups or phenyl ring in BDSA. C3 polymer unit had a side chain length that is optimal for bridging the acid anhydride monomers, stabilizing the dimerized state of sulfonic acid groups. In contrast, the side chain was too short in C0 polymer unit, whereas the side chains in C6 and C10 polymer units are too long, resulting in the destabilization of the dimerized state of the sulfonic acid groups. As shown in Figure 7(b), the C3 thin film showed higher proton conductivity than longer-side chain analogue C6 or C10 thin film at a low humidification range ($\lambda < 4$). Also, the proton conductivity of C3 thin film was comparable with that of lower p K_a analogue C0 thin film at $\lambda \sim 4$. The calculation results showed that the side chain of C3 has an appropriate length to form a close contact of the sulfonic acid groups in a hydrophobic environment. This result could be one factor to explain the high proton conductivity of C3 thin film in the lower hydrated state.

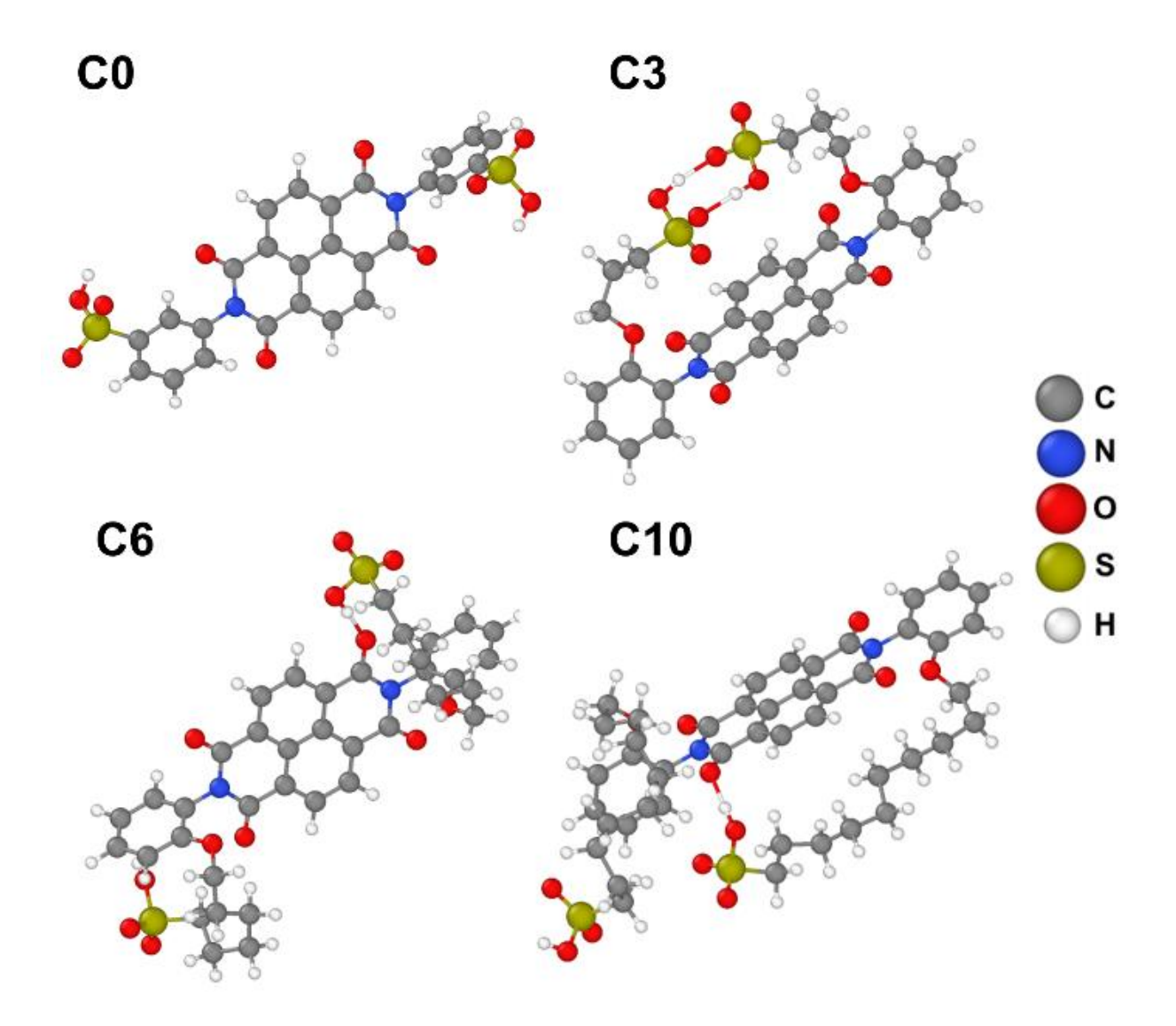


Figure 8. Stable conformations of **C0**, **C3**, **C6** and **C10** polymer units. Black: carbon; blue: nitrogen; red: oxygen; yellow: sulfur, white: hydrogen.

The results of this study illustrate the significant impact of alkyl side chain length on the structural organization and proton conductivity of SPI thin films. Using various analytical techniques, it was found that all SPI thin films formed lyotropic lamellar structures upon hydration, with lamellar spacing increasing with longer alkyl side chains. This structural organization was consistent across all samples, as evidenced by IR pMAIRS results showing parallel backbone

alignment to the substrate. Water uptake varied with side chain length, with the C0 thin film exhibiting the highest uptake and the C10 thin film the lowest due to differences in hydrophilicity and possessing high oxidation durability. Proton conductivity measurements revealed that C3, with a three-carbon alkyl side chain, achieved the highest proton conductivity and lowest activation energy, attributed to its optimal side chain length, facilitating efficient proton transport. Computational analysis supported these findings, demonstrating that C3's side chain length was ideal for bridging acid anhydride monomers and advantageous in high proton conduction at low hydration state.

4. Conclusion

This study systematically examined the effects of varying alkyl side chain lengths on the structural organization and proton conductivity of SPI thin films. The formation of lamellar structures was confirmed across all SPI thin films, with lamellar spacing increasing as the length of the alkyl side chain increased. GIXRS measurements showed that the lyotropic lamellar spacing increased with humidification; the spacing for $\bf C0$ thin film increased from 0.67 nm to 2.2 nm. The lamellar spacing increased as the alkyl chain increased, and for $\bf C10$ thin film, it reached 5.1 nm at 95% RH. At the same water uptake amount ($\lambda = 10$) or at the highest RH, the lamellar spacing exhibited a nearly linear relationship with the number of carbon atoms in the side chain, indicating that side chain length directly influences the structural organization. Additionally, IR pMAIRS results indicated that the backbone alignment was consistent across all SPI thin films, with the polymer backbones oriented parallel to the substrate irrespective of the side chain length. This uniform alignment plays a crucial role in maintaining the structural integrity and facilitating proton transport.

Water uptake behavior was significantly influenced by the alkyl side chain length. QCM measurements demonstrated that the **C0** thin film showed higher water uptake at lower RH levels compared to other SPIs, while the **C10** thin film exhibited the lowest water uptake due to its lower hydrophilicity and possessing high oxidation durability. Proton conductivity measurements revealed that the **C3** thin film displayed the highest proton conductivity at high humidity levels, reaching 1.8×10^{-1} S cm⁻¹ at 95% RH and 25°C. The conductivity decreased with increasing alkyl side chain length, with the **C0** thin film showing 7.5×10^{-2} S cm⁻¹, the **C6** thin film at 9.6×10^{-2} S cm⁻¹, and the **C10** thin film at 3.4×10^{-2} S cm⁻¹.

In situ FTIR analysis showed that the proton dissociation rate from sulfonic acid groups varied with side chain length and humidity. The **C0** thin film had a higher proton dissociation rate at lower humidity levels compared to the other SPIs, attributed to its lower pK_a value (-2.5). This higher dissociation rate contributed to its superior proton conductivity at low humidity. The presence of alkyl side chains influenced the Vehicle and Grotthuss mechanisms of proton transport, with **C3** providing optimal conditions for efficient proton conduction due to its balanced side chain length, which was supported by theoretical calculations.

Overall, this research elucidates the critical role of alkyl side chain length in determining the structural and proton conductive properties of SPI thin films. By understanding and manipulating these molecular characteristics, the performance of SPIs in energy applications can be optimized. These findings provide a valuable framework for designing advanced materials with enhanced proton transport efficiencies.

ASSOCIATED CONTENT

The Supporting Information is available free of charge on the https://pubs.acs.org/. Synthesis of monomer and polyimides with different alkyl side chain lengths, Fenton test, RH controlled GIXRS, temperature dependent proton conductivity, RH controlled FTIR measurements, computational conformation analysis in function of side chain lengths.

AUTHOR INFORMATION

Corresponding Author

*ynagao@jaist.ac.jp

Present Addresses

M. H.: Faculty of Engineering and Design, Kagawa University, 2217-20 Hayashicho, Takamatsu, Kagawa 761-0396, Japan

Funding Sources

Y. N. appreciated the support by JSPS KAKENHI grant number JP21H01997. M. H., A. T., K. A., S. N., M. K., and Y. N. thanked the financial support by JST CREST Grant Number JPMJCR21B3, Japan.

Notes

The authors declare that they have no competing financial interest.

ACKNOWLEDGMENT

We acknowledge Prof. Tomohiro Yasuda from Hokkaido University for guiding synthesis of BSHB and BSDB monomers.

ABBREVIATIONS

NTDA, 1,4,5,8-naphthalenetetracarboxylic dianhydride; BDSA, 2,2'-benzidinedisulfonic acid, BSPB, 3,3'-bis(sulfopropoxy)benzidine; BSHB, 3,3'-bis(6-sulfohexyloxy)benzidine; BSDB, 3,3'-bis(10-sulfodecyloxy)benzidine; TEA, triethylamine; DMSO, dimethyl sulfoxide; SPI, sulfonated polyimide; LC, liquid crystalline; RH, relative humidity; NMR, nuclear magnetic resonance; FTIR, Fourier transform infrared; ATR, attenuated total reflectance; GPC, gel permeation chromatography; WIM, white light interferometer; AFM, atomic force microscope; IR pMAIRS, infrared p-polarized multiple angle incidence resolution spectrometry; POM, polarized optical microscopy; QCM, quartz crystal microbalance; EW, equivalent weight; GIXRS, grazing-incidence X-ray scattering; IP, in-plane; OP, out-of-plane, AC, alternating current; ETKDG, experimental-torsion-knowledge distance geometry; L-BFGS, limited-memory Broyden-Fletcher-Goldfarb-Shanno; UNNP, universal neural network potential; PFP, PreFerred potential.

REFERENCES

- 1. Nagao, Y. Proton-Conducting Polymers: Key to Next-Generation Fuel Cells, Electrolyzers, Batteries, Actuators, and Sensors. *ChemElectroChem* **2024**, *11*, e202300846.
- 2. Shin, D. W.; Guiver, M. D.; Lee, Y. M. Hydrocarbon-Based Polymer Electrolyte Membranes: Importance of Morphology on Ion Transport and Membrane Stability. *Chem. Rev.* **2017**, *117*, 4759-4805.
- 3. Rikukawa, M.; Sanui, K. Proton-Conducting Polymer Electrolyte Membranes Based on Hydrocarbon Polymers. *Prog. Polym. Sci.* **2000**, *25*, 1463-1502.
- 4. Kreuer, K. D. On the Development of Proton Conducting Polymer Membranes for Hydrogen and Methanol Fuel Cells. *J. Membr. Sci.* **2001**, *185*, 29-39.
- 5. Hickner, M. A.; Ghassemi, H.; Kim, Y. S.; Einsla, B. R.; McGrath, J. E. Alternative Polymer Systems for Proton Exchange Membranes (Pems). *Chem. Rev.* **2004**, *104*, 4587-4611.
- 6. Yang, Y.; Holdcroft, S. Synthetic Strategies for Controlling the Morphology of Proton Conducting Polymer Membranes. *Fuel Cells* **2005**, *5*, 171-186.
- 7. Zhang, H.; Shen, P. K. Recent Development of Polymer Electrolyte Membranes for Fuel Cells. *Chem. Rev.* **2012**, *112*, 2780-2832.
- 8. Lee, K. H.; Chu, J. Y.; Kim, A. R.; Yoo, D. J. Enhanced Performance of a Sulfonated Poly(Arylene Ether Ketone) Block Copolymer Bearing Pendant Sulfonic Acid Groups for

- Polymer Electrolyte Membrane Fuel Cells Operating at 80% Relative Humidity. *ACS Appl. Mater. Interfaces* **2018**, *10*, 20835-20844.
- 9. Lim, D.-W.; Kitagawa, H. Proton Transport in Metal-Organic Frameworks. *Chem. Rev.* **2020**, 120, 8416-8467.
- 10. Li, W.-H.; Deng, W.-H.; Wang, G.-E.; Xu, G. Conductive Mofs. *EnergyChem* **2020**, *2*, 100029.
- 11. Nagao, Y. Advancing Sustainable Energy: Structurally Organized Proton and Hydroxide Ion-Conductive Polymers. *Curr. Opin. Electrochem.* **2024**, *44*, 101464.
- 12. Trigg, E. B.; Winey, K. I. Nanoscale Layers in Polymers to Promote Ion Transport. *Mol. Syst. Des. Eng.* **2019**, *4*, 252-262.
- 13. Uchida, J.; Soberats, B.; Gupta, M.; Kato, T. Advanced Functional Liquid Crystals. *Adv. Mater.* **2022**, *34*, 2109063.
- 14. Oshiro, H.; Kobayashi, T.; Ichikawa, T. Molecular Design of a Series of Gemini-Type Zwitterionic Amphiphiles with Various Linker Lengths: Control of Their Self-Organisation for Developing Gyroid Nanostructured Proton Conductive Membranes. *Mol. Syst. Des. Eng.* **2022**, 7, 1459-1466.
- 15. Ichikawa, T.; Yamada, T.; Aoki, N.; Maehara, Y.; Suda, K.; Kobayashi, T. Surface Proton Hopping Conduction Mechanism Dominant Polymer Electrolytes Created by Self-Assembly of Bicontinuous Cubic Liquid Crystals. *Chem. Sci.* **2024**, *15*, 7034-7040.
- 16. Luo, J.; You, J.; Tan, S.; Wang, C.; Wu, Y. Lamellar Lyotropic Liquid Crystal Superior to Micellar Solution for Proton Conduction in an Aqueous Solution of 1-Tetradecyl-3-
- Methylimidazolium Hydrogen Sulfate. ACS Appl. Mater. Inter. 2020, 12, 45611-45617.
- 17. Yao, Y.; Watanabe, H.; Hara, M.; Nagano, S.; Nagao, Y. Lyotropic Liquid Crystalline Property and Organized Structure in High Proton-Conductive Sulfonated Semialicyclic Oligoimide Thin Films. *ACS Omega* **2023**, *8*, 7470-7478.
- 18. Goto, R.; Ono, Y.; Hara, M.; Seki, T.; Nagao, Y.; Nagano, S. Preparation and Structural Characterization of Shear-Aligned Films in a High Proton Conductive Alkyl-Sulfonated Polyimide with Lyotropic Liquid Crystallinity. *Mol. Cryst. Liq. Cryst.* **2021**, *727*, 23-32.
- 19. Krishnan, K.; Iwatsuki, H.; Hara, M.; Nagano, S.; Nagao, Y. Proton Conductivity Enhancement in Oriented, Sulfonated Polyimide Thin Films. *J. Mater. Chem. A* **2014**, *2*, 6895-6903.
- 20. Nagao, Y. Progress on Highly Proton-Conductive Polymer Thin Films with Organized Structure and Molecularly Oriented Structure. *Sci. Tech. Adv. Mater* **2020**, *21*, 79-91.
- 21. Ono, Y.; Goto, R.; Hara, M.; Nagano, S.; Abe, T.; Nagao, Y. High Proton Conduction of Organized Sulfonated Polyimide Thin Films with Planar and Bent Backbones. *Macromolecules* **2018**, *51*, 3351-3359.
- 22. Hasegawa, T. Advanced Multiple-Angle Incidence Resolution Spectrometry for Thin-Layer Analysis on a Low-Refractive-Index Substrate. *Anal. Chem.* **2007**, *79*, 4385-4389.
- 23. Hasegawa, T.; Shioya, N. Mairs: Innovation of Molecular Orientation Analysis in a Thin Film. *Bull. Chem. Soc. Jpn.* **2020**, *93*, 1127-1138.
- 24. Yasuda, T.; Li, Y.; Miyatake, K.; Hirai, M.; Nanasawa, M.; Watanabe, M. Synthesis and Properties of Polyimides Bearing Acid Groups on Long Pendant Aliphatic Chains. *Journal of Polymer Science Part A: Polymer Chemistry* **2006**, *44*, 3995-4005.
- 25. Miyatake, K.; Yasuda, T.; Hirai, M.; Nanasawa, M.; Watanabe, M. Synthesis and Properties of a Polyimide Containing Pendant Sulfophenoxypropoxy Groups. *Journal of Polymer Science Part A: Polymer Chemistry* **2007**, *45*, 157-163.

- 26. Wang, S.; Witek, J.; Landrum, G. A.; Riniker, S. Improving Conformer Generation for Small Rings and Macrocycles Based on Distance Geometry and Experimental Torsional-Angle Preferences. *J. Chem. Inf. Model.* **2020**, *60*, 2044-2058.
- 27. Hawkins, P. C. D. Conformation Generation: The State of the Art. J. Chem. Inf. Model. 2017, 57, 1747-1756.
- 28. Riniker, S.; Landrum, G. A. Better Informed Distance Geometry: Using What We Know to Improve Conformation Generation. *J. Chem. Inf. Model.* **2015**, *55*, 2562-2574.
- 29. The Rdkit: Open-Source Cheminformatics Software, Version 2023.09.6. Github, 2019; Https://Www.Rdkit.Org.
- 30. Takamoto, S.; Shinagawa, C.; Motoki, D.; Nakago, K.; Li, W.; Kurata, I.; Watanabe, T.; Yayama, Y.; Iriguchi, H.; Asano, Y.; Onodera, T.; Ishii, T.; Kudo, T.; Ono, H.; Sawada, R.; Ishitani, R.; Ong, M.; Yamaguchi, T.; Kataoka, T.; Hayashi, A.; Charoenphakdee, N.; Ibuka, T. Towards Universal Neural Network Potential for Material Discovery Applicable to Arbitrary Combination of 45 Elements. *Nat. Commun.* **2022**, *13*, 2991.
- 31. Grimme, S.; Ehrlich, S.; Goerigk, L. Effect of the Damping Function in Dispersion Corrected Density Functional Theory. *J. Comput. Chem.* **2011**, *32*, 1456-1465.
- 32. Grimme, S.; Antony, J.; Ehrlich, S.; Krieg, H. A Consistent and Accurate Ab Initio Parametrization of Density Functional Dispersion Correction (Dft-D) for the 94 Elements H-Pu. *J. Chem. Phys.* **2010**, *132*, 154104.
- 33. *Matlantis* (<u>Https://Matlantis.Com/</u>), Software as a Service Style Material Discovery Tool.
- 34. Stukowski, A. Visualization and Analysis of Atomistic Simulation Data with Ovito-the Open Visualization Tool. *Modelling Simul. Mater. Sci. Eng.* **2010**, *18*, 015012.
- 35. Krishnan, K.; Iwatsuki, H.; Hara, M.; Nagano, S.; Nagao, Y. Influence of Molecular Weight on Molecular Ordering and Proton Transport in Organized Sulfonated Polyimide Thin Films. *J. Phys. Chem. C* **2015**, *119*, 21767-21774.
- 36. Hofmann, D. W. M.; Kuleshova, L.; D'Aguanno, B.; Di Noto, V.; Negro, E.; Conti, F.; Vittadello, M. Investigation of Water Structure in Nafion Membranes by Infrared Spectroscopy and Molecular Dynamics Simulation. *J. Phys. Chem. B* **2009**, *113*, 632-639.
- 37. Brubach, J.-B.; Mermet, A.; Filabozzi, A.; Gerschel, A.; Roy, P. Signatures of the Hydrogen Bonding in the Infrared Bands of Water. *J. Chem. Phys.* **2005**, *122*, 184509.
- 38. Heitner-Wirguin, C. Infra-Red Spectra of Perfluorinated Cation-Exchanged Membranes. *Polymer* **1979**, *20*, 371-374.
- 39. Buzzoni, R.; Bordiga, S.; Ricchiardi, G.; Spoto, G.; Zecchina, A. Interaction of H2o, Ch3oh, (Ch3)2o, Ch3cn, and Pyridine with the Superacid Perfluorosulfonic Membrane Nafion: An Ir and Raman Study. *The Journal of Physical Chemistry* **1995**, *99*, 11937-11951.
- 40. Chang, Y.; Brunello, G. F.; Fuller, J.; Hawley, M.; Kim, Y. S.; Disabb-Miller, M.; Hickner, M. A.; Jang, S. S.; Bae, C. Aromatic Ionomers with Highly Acidic Sulfonate Groups: Acidity, Hydration, and Proton Conductivity. *Macromolecules* **2011**, *44*, 8458-8469.

Table of contents:

